

# The Challenge of Electrolyte Impregnation in the Fabrication and Operation of Li-ion and Li–S Batteries

Matthew Dent,<sup>[a]</sup> Sean Grabe,<sup>[a]</sup> and Constantina Lekakou<sup>\*[b]</sup>

Modeling and simulations, coupled with selected experimental studies for validation, are employed to analyze electrolyte impregnation in battery fabrication, elucidate and assess its effects on battery operation. Digital twins of the electrolyte filling process or the cell cycling are based on continuum-level physicochemical models taking into account the pore size distribution of the porous cathode and separator, dissolution and precipitation of any solutes such as sulfur or sulfides; additionally, ion transport and redox reactions in the liquid

electrolyte for simulations of battery cycling. Electrolyte impregnation highly depends on cell format, with a cylindrical Li-ion cell predicted to take up to 7 days under rest for homogeneous electrolyte distribution. Simulations of the electrolyte infiltration in Li–S coin cells revealed sulfur dissolution and reprecipitation, which was verified by experiments using *in operando* microscopy. Simulations of the first discharge of electrolyte-lean Li–S cells demonstrated the effects of poor micropore wetting by the electrolyte.

## Introduction

Electrolyte infiltration is a crucial process step in batteries that affects their performance and cost. Liquid electrolytes are preferred compared to solid electrolytes, as the latter exhibit limited ion diffusivity which reduces the specific capacity and power density of the battery or supercapacitor.<sup>[1]</sup> The liquid electrolyte accounts for about 15 wt% of the cell mass for Li-ion batteries<sup>[2–4]</sup> but for devices with mesoporous electrodes the amount of electrolyte is higher, reaching 50 wt% of the mass of a large supercapacitor pouch cell.<sup>[5,6]</sup> Reducing the electrolyte mass is a key aim to improve the gravimetric energy and power densities of future battery technologies, with a target of E/S (electrolyte to sulfur) ratio of 5 µl of electrolyte per mg of sulfur for Li–S batteries.<sup>[7]</sup> This was further reduced to 2.4 µl/mg<sub>S</sub> in fabricated pouch cells with a cathode of 70 wt% S in Li<sub>x</sub>MoS<sub>2</sub> that reached an energy density of 440 Wh/kg of cell mass<sup>[8]</sup> but even this small amount accounted for 46 wt% of the Li–S pouch cell.<sup>[8]</sup>

The aim in all battery and supercapacitor technologies is that the electrolyte fully wets the surface area of electrodes and

separator of all pores in which the electrolyte ions and other ions of interest can enter and be accommodated.<sup>[9–12]</sup> Wetting properties of electrolyte against electrode and separator materials, such as the contact angle, are a critical factor in this aspect. Depending on the amount of the added electrolyte, the local degree of infiltration and the pore size distribution (PSD) of each material in the cell, each porous material may be locally fully or partially saturated with electrolyte.<sup>[13–15]</sup> The focus in this study is on how the electrolyte infiltration stage during cell manufacture affects the distribution of the electrolyte and degree of saturation throughout the cell.

The cell format is an important factor in the infiltration of electrolyte at cell fabrication. Laboratory-made coin cells usually involve inserting the electrolyte drop-by-drop on the top surface of a layer (electrode or separator); then electrolyte filling takes place via the transverse cell direction and is fast through the small cell thickness.<sup>[16]</sup> Electrolyte injection in pouch and prismatic cells takes place on the side, so electrolyte filling occurs in the in-plane direction with secondary flow in the transverse direction. In general, as infiltration in pouch cells is usually under vacuum, the degree of compression is low and the interlayer porosity and resulting permeability is relatively high, so good infiltration can be achieved,<sup>[17]</sup> following classical composite manufacturing techniques under flexible tool.<sup>[18]</sup> In cylindrical cells electrolyte is injected from the top or a side-position near the top, in which case electrolyte filling takes place longitudinally with secondary flow in the transverse direction. Due to the higher compression of wound layers in cylindrical cells compared to pouch cells and the long length of the former compared to the small thickness of coin cells, cylindrical cells could be considered the most difficult cell format for electrolyte infiltration. The tightly wound electrode and separator layers in the cylindrical cells have reduced permeability and may also generate higher local solid fractions inhibiting electrolyte infusion.

The degree of saturation of electrolyte changes during battery cell cycling, with particular effects observed in some cell

[a] M. Dent, S. Grabe  
School of Mechanical Engineering Sciences  
University of Surrey  
Guildford, Surrey GU2 7XH, UK  
E-mail: m.j.dent@surrey.ac.uk  
sg00566@surrey.ac.uk

[b] Prof. C. Lekakou  
School of Mechanical Engineering Sciences  
University of Surrey  
Guildford, Surrey GU2 7XH, UK  
E-mail: C.lekakou@surrey.ac.uk

Supporting information for this article is available on the WWW under <https://doi.org/10.1002/batt.202300327>

© 2023 The Authors. *Batteries & Supercaps* published by Wiley-VCH GmbH. This is an open access article under the terms of the Creative Commons Attribution License, which permits use, distribution and reproduction in any medium, provided the original work is properly cited.

formats. SEI formation, especially thick deposits in severe cases of aging,<sup>[19]</sup> readjust the distribution of electrolyte and wetting. Cycling expansion and contraction of cells is observed in both Li-ion and Li–S cells, where in the latter a maximum sulfur expansion of 70% is expected in the cathode in its ultimate conversion to  $\text{Li}_2\text{S}$  at the end of discharge. Pouch cells are able to accommodate such expansion but confined cell formats, especially cylindrical cells exhibit serious layer deformation, folding and even fracture near their centerline<sup>[20]</sup> with corresponding changes in the degree of electrolyte saturation. In Li–S batteries, dissolution and precipitation of sulfur and polysulfides takes place in the electrolyte during cell cycling,<sup>[21]</sup> continuously changing the local porosity and pore size distribution, which results in continuous redistribution of electrolyte.

With regards to the modeling and simulation of electrolyte infiltration, there are several approaches that may be recommended. Infiltration of a liquid through a porous medium is described by the classical Darcy's law in a continuum model that may also include capillary pressure effects. It is commonly employed for simulations of composites manufacturing, in which a single pore model or dual pore model (macropores between fiber bundles and micropores between microfibers in a bundle) is usually applied.<sup>[22]</sup> For more complex pore architectures, as in the case of battery electrodes, a three-dimensional-resolved lattice Boltzmann model is more accurate, taking into account the effects of porosity, pore size distribution and pores interconnectivity on the filling dynamics using the full Navier-Stokes equations.<sup>[23,24]</sup> However, these simulations are very time-consuming and the results depend very much on an accurate imported pore architecture, usually employing X-ray microtomography. The long simulation time and large amount of required memory allow the electrolyte infiltration to be analyzed only for a small volume inside the battery cell,<sup>[23]</sup> rather than the full length of a cylindrical or pouch cell. For these reasons, our group has developed a novel continuum, volume averaged infiltration model<sup>[14]</sup> taking into account the pore size distribution of the porous medium that can be measured with the more commonly available method of  $\text{N}_2$  adsorption. This simulation method assumes a pore connectivity model, usually hierarchical pore size-based connectivity or other defined model if certain features are known, for example hollow particles or hollow fibers.<sup>[25]</sup>

Modeling the dynamics of ion transport and electrochemical processes for mesoporous electrodes during battery cycling becomes even more complex, given the much larger number of equations to describe various electrochemical processes and physical processes, such as sulfur and sulfides dissolution and precipitation in sulfur batteries. Well known models have assumed a single pore size for each electrode, such as Kumaresan's model for Li–S batteries.<sup>[26]</sup> This was extended to a dual pore-size model, with macropores between particles and micropores inside particles.<sup>[27]</sup> More time-consuming three-dimensional kinetic Monte Carlo simulations of Li–S cathode were also conducted for an *in silico* created cathode model consisting of *in silico* model of carbon spheres coated by sulfur.<sup>[28]</sup> All such studies have been qualitative, with almost no

direct comparison between computational and experimental results, presumably due to the high degree of assumption in the model and cathode pore structure. X-ray microtomography methods, to detect the detailed pore architecture in the electrode and monitor sulfur dissolution and precipitation, reach a resolution limit of 500 nm at best,<sup>[21]</sup> which means they cannot detect the micropores and mesopores of cathode hosts of sulfur batteries, which are critical in the retention or the migration and shuttling of soluble polysulfides. Hence, our group has developed a novel continuum, volume averaged model for the cycling of Li–S batteries, taking into account the pore size distribution of the porous cathode that can be easily determined via  $\text{N}_2$  adsorption tests detecting pores down to 0.3 nm. This model has been successfully validated against experimental data for Li–S batteries with different types of cathode hosts, including activated carbon fiber fabric,<sup>[10]</sup> activated carbon coating,<sup>[25]</sup> graphene coating<sup>[25]</sup> and hollow activated carbon particle coating.<sup>[25]</sup> All physicochemical battery models reported so far have assumed saturated porous media (electrodes, separator). The present study is the first investigation including a model for the cycling of Li–S battery in unsaturated porous medium, where the degree of electrolyte saturation is locally updated as a function of time during battery cell operation.

The focus of this study is investigating the impregnation of electrolyte for Li-ion and Li–S cells at the fabrication stage for two cell formats: laboratory-made coin cell for Li–S batteries the development of which is still in early stages and most data in the literature come from coin cells; and a cylindrical cell for Li-ion batteries which is the case for most commercial Li-ion cells and is the most difficult cell format for electrolyte infiltration. The selection of these two distinct lithium technologies was based on the differences regarding their electrode porosity and pore size distribution. Li-ion batteries generally feature dense anode and cathode active materials, requiring only a small amount of electrolyte (about 15 wt% of the cell mass<sup>[2–4]</sup>) to wet them and facilitate  $\text{Li}^+$  ion transport during battery operation. For this reason, it would be interesting to investigate in simulations whether and how rapidly homogeneous wetting of the electrodes by the electrolyte might be realized, with the focus on the cylindrical cell format in which the tightly wound material layers are under the highest degree of compression. The LFP-graphite based Li-ion battery was selected for the simulations as an example of a typical Li-ion battery, well established commercially in the format of cylindrical cells and with a good amount of experimental data in the literature. Li–S batteries have generally highly mesoporous cathode hosts to accommodate the sulfur and sulfides. For this reason, a much larger amount of liquid electrolyte is needed (about 45–50 wt% of the cell mass<sup>[8]</sup>) for the wetting of the large surface area of cathode, while sulfur and sulfides can also dissolve in the electrolyte or precipitate if their local concentration exceeds the saturation limit. Simulation of the electrolyte infiltration becomes more complex to include sulfur dissolution and precipitation dynamics. In this case, the interest is in the degree of electrolyte saturation across the cell after the electrolyte infiltration.

Digital twins are employed for these simulations based on continuum, volume averaged physicochemical models taking into account the pore size distribution of the porous medium. The general case of an unsaturated porous medium is modeled where the distribution of the degree of electrolyte saturation is monitored during the simulations across the main cell dimension and for different pore sizes. For the first time in the literature, a novel model for Li–S battery cells is presented considering unsaturated porous cathode and separator and taking into account the pore size distribution which may change with time due to dissolution and precipitation of sulfur and sulfides. Parametric simulations will be conducted for different amounts of added electrolyte with respect to the amount of sulfur in the cathode (different E/S ratios) of Li–S battery cells to investigate the distribution of the degree of saturation of the electrolyte at the end of electrolyte infiltration, and its subsequent effects during the cycling of the Li–S battery cell. The simulations are linked to experimental data from this study.

## Modeling

A three-phase model is considered for the electrodes and other layers (separator, interlayers) of battery cells, comprising: the solid phase, the void phase and the liquid electrolyte phase characterized by its degree of saturation,  $S_e$ , defined as the volume fraction of electrolyte with respect to the non-solid volume. The solid phase of electrodes or separator is characterized by a pore size distribution, inputted in discretized form in the models of this study. Each pore size  $p$  has a solid phase volume fraction  $\alpha_{s,p}$  and a pore volume fraction  $\varepsilon_p$  so that

$$\alpha_{s,p} + \varepsilon_p = 1 \quad (1)$$

where the pore fraction contains a subfraction  $S_{e,p}$  of electrolyte and a void subfraction  $S_{v,p} = 1 - S_{e,p}$ .

A three-dimensional mass transport equation is considered for the electrolyte as a function of time,  $t$ , in each pore size  $p$  taken from the local PSD of the solid medium (electrode, separator, interlayers):

$$\frac{\partial(\varepsilon_p S_{e,p})}{\partial t} + \nabla \cdot (\mathbf{U} \varepsilon_p S_{e,p}) = 0 \quad (2)$$

where each component of the velocity vector  $\mathbf{U}$  is given by Darcy's law:

$$U_i = - \frac{K_p}{\varepsilon_p \mu_e} \frac{\partial P}{\partial x_i} \quad (3)$$

where  $\mu_e$  is the electrolyte viscosity and  $K_p$  is the permeability of the porous medium for each pore size  $p$  given by the Carman-Kozeny equation for flow through a porous bed of spherical particles of pore size  $d_p$ .<sup>[29]</sup>

$$K_p = \frac{\varepsilon_p d_p^2}{16 \times 7.5} \quad (4)$$

$\partial P / \partial x_i$  is the pressure drop, which is assumed to vary linearly in each  $x_i$  direction between the inlet boundary condition  $P_{inj}$  (with the possibility that  $P_{inj} = 0$ ) and the boundary condition at the flow front  $P_{ff} = P_v + P_{c,p}$ , with vacuum pressure  $P_v$  if this is the case and capillary pressure  $P_{c,p}$  given by the Young-Laplace equation:<sup>[22,30]</sup>

$$P_{c,p} = \frac{4\sigma_e \cos\gamma}{d_p} \quad (5)$$

where  $\sigma_e$  and  $\gamma$  are the surface tension of electrolyte and its contact angle with the solid porous medium. The following data has been used for the electrolytes in the simulations of this study. For electrolytes DOL/DME, 1:1 v/v for Li–S batteries and Li-ion electrolytes EC/DMC and EC/EMC 1:1 v/v, surface tension:  $\sigma_{DOL/DME} = 28.68 \text{ mN m}^{-1}$ ,<sup>[31,32]</sup>  $\sigma_{EC/DMC} = 40.13 \text{ mN m}^{-1}$ ,  $\sigma_{EC/EMC} = 34.61 \text{ mN m}^{-1}$ ,<sup>[13]</sup> and contact angle with polyolefinic separator:  $\gamma_{DOL/DME\_Sep} = 44.7^\circ$ ,<sup>[33]</sup>  $\gamma_{EC/DMC\_Sep} = 52.9^\circ$ ,  $\gamma_{EC/EMC\_Sep} = 45.4^\circ$ ,<sup>[13]</sup> with a carbon-sulfur cathode surface:  $\gamma_{DOL/DME-C/S} = 20^\circ$ ,<sup>[34]</sup> with NMC cathode:  $\gamma_{EC/EMC-NMC} = 10.6^\circ$ ,<sup>[35]</sup> PVDF binder  $\gamma_{EC/DMC-PVDF} = 25^\circ$ ,<sup>[36]</sup> and with graphite anode:  $\gamma_{EC/EMC-Graphite} = 22.8^\circ$ ,<sup>[35]</sup>

In Li–S or other metal-sulfur batteries, sulfur is also dissolved in the electrolyte solution at concentration,  $C_{S8,p}$  in each pore size  $p$ , and transported in the system according to its mass transport equation:

$$\frac{\partial(\varepsilon_p C_{S8,p})}{\partial t} + \nabla \cdot (\mathbf{U} \varepsilon_p C_{S8,p}) = \nabla \cdot (D_{S8,p} \nabla(\varepsilon_p C_{S8,p})) + \frac{\partial^2 m_{S8}}{\partial t \partial V} \quad (6)$$

under the effect of convection and diffusion, with  $D_{S8,p}$  being the diffusion coefficient of  $S_8$  in the electrolyte solution in pore size  $p$ , expressed by the Stokes-Einstein relation:<sup>[11,12,37]</sup>

$$D_{S8,p} = \frac{k_B T}{3\pi\mu d_{S8}} \quad (7)$$

where  $T$  is the absolute temperature,  $k_B$  the Boltzmann's constant and  $d_{S8}$  is the size of the  $S_8$  molecule in solvated form or desolvated form if pore size  $p$  is smaller than the solvated  $S_8$  molecule, with molecule sizes supplied from molecular simulations.<sup>[9]</sup>

The last term in equation (6) is the dissolution rate of  $S_8$  per volume, where the dissolution rate is given by the equation:<sup>[14,38,39]</sup>

$$\frac{\partial m_{S8}}{\partial t} = k_{S8} A (C_{S8-sat} - C_{S8,p}) \quad (8)$$

where  $C_{S8-sat}$  is the saturation concentration of  $S_8$  in the electrolyte solution,  $k_{S8}$  is the mass transfer coefficient of  $S_8$  from solid to solution phase and  $A$  is the interfacial pore area.

The system of equations (1)–(8) describes the electrolyte impregnation during the cell fabrication stage and electrolyte

flow rearrangements during the battery cell operation, where the porosity and pore size change locally.

During the operation of a Li–S battery simulated in this study, for low E/S ratios that result in cathode and separator layers unsaturated by the liquid electrolyte, the general species equation is given by the equation:

$$\frac{\partial \varepsilon_p S_{e,p} \alpha_{s,p}}{\partial t} - \frac{z_s}{F N_A V_s} \frac{\partial}{\partial x} \left( i_e F_{s,Decay} t_{s,p} S_{e,p} \alpha_{s,p} \right) = \frac{\partial}{\partial x} \left( \varepsilon_p S_{e,p} D_{s,p} F_{s,Decay} \frac{\partial \alpha_{s,p}}{\partial x} \right) + \frac{I_{s,p-1/p} - I_{s,p/p+1}}{\Delta x} + S_{e,p} r_{s,p} + S_{e,p} R_{s,p} \quad (9)$$

where  $\alpha_{s,p}$  is the volume fraction of species S in the electrolyte of pore size p,  $z_s$  is the number of transferred electrons for species S, F is the Faraday constant,  $N_A$  is the Avocadro number,  $V_s$  is the volume of ion or molecule of species S,  $i_e$  is the current density of the electrolyte phase,  $t_{s,p}$  is the transference number of species S in the electrolyte phase of pore size p,  $r_{s,p}$  is the sum of the rates of all electrochemical reactions involving species S in the liquid electrolyte phase in pore size p<sup>[10]</sup> and  $R_{s,p}$  is the net rate between the rate of dissolution and the rate of precipitation of species S in pore size p.<sup>[10,25]</sup> The current flux of ions or molecules S from pore p-1 to pore p is given by:

$$I_{s,p-1/p} = F_{s,decay} \frac{\varepsilon_{p-1} S_{e,p-1} d_p^2 z_s N_A V_s t_{s,p} i_e}{\varepsilon_p S_{e,p} d_{p-1}^2} \quad (10)$$

For unsaturated solid media, it is considered that ions and molecules in the liquid electrolyte phase exist and are transported within the electrolyte layer wetting the pore wall of pore size p rather than within the whole pore size  $d_p$  if the pore was fully saturated. The diffusion coefficient of species S in the liquid electrolyte phase of pore size p is given by the relation:

$$D_{s,p} = \frac{\delta_{s,p} k_B T}{2 \pi \mu_e \varepsilon_p^{1.5} (d_{solv,S} \text{ or } d_S)} \quad (11)$$

where  $d_{solv,S}$  and  $d_S$  are the size of the solvated and desolvated ion or molecule of species S,<sup>[9]</sup> depending on which fits the pore size  $d_p$  for saturated pores ( $S_{e,p}=1$ ) or the thickness  $d_{el-layer}$  of the electrolyte layer wetting the pore surface for unsaturated pores ( $S_{e,p}<1$ ). The constrictivity  $\delta_{s,p}$  is given by the relation:

$$\delta_{s,p} = \left( 1 - \frac{d_{solv,S} \text{ or } d_S}{d_p \text{ or } d_{el-layer}} \right)^4 \quad (12)$$

$F_{s,Decay}$  in equations (9) and (10) is the decay factor<sup>[10,11,25]</sup> applied in case:  $d_S < d_p$  or  $d_{el-layer} < d_{solv,S}$ . Table SI-1 presents all equations employed for the simulation of the Li–S battery cell cycling, including equations (9)–(12) above, the rest of equations of the electrochemical model, model of the dissolution and precipitation of species, and models for the solution properties changing dynamically during the cycling of a Li–S cell.

## Results and Discussion

First of all, simulations of the electrolyte infiltration were carried out for a graphite-LFP Li-ion cell of 26650 cylindrical format. The cylindrical cell format was selected as this is the most difficult cell type for electrolyte impregnation due to the highest layer compression and, hence, lowest permeability. The focus was on adjacent anode, separator and cathode layers from the jelly roll of the full cylindrical cell, with experimental data of the PSD extracted by Scipioni et al<sup>[40]</sup> from the 3D-reconstructed microstructure of electrodes based on FIB/SEM images of cross-sections in their study.<sup>[40]</sup> The PSD of the separator was extracted from SEM image for the present study and presented in Figure SI-1(a). Although  $N_2$  adsorption experiments are typically used to determine the PSD of microporous materials, other methods such as SEM or X-ray micro-CT<sup>[4,21]</sup> might be used if the pore sizes are within the resolution of the method: this happens to be the case for the typical electrodes of Li-ion batteries<sup>[4,40]</sup> but not for the highly microporous electrode hosts of Li–S batteries or the electrodes of supercapacitors. In such cases,  $N_2$  adsorption measurements are preferred as they are able to detect pores down to 0.3 nm.<sup>[10–12,25]</sup>

The results of contour plots of the local degree of saturation of electrolyte as a function of the radial location through the graphite-LFP cell thickness and the pore size are depicted in Figure 1. It must be noted that the radial distance starts at  $r_o = 1.8$  mm near the centerline of the 26650 cylindrical cell. The PSD of the anode is in the range of 2.8 to 590 nm, the PSD of the separator is in the range of 19 to 140 nm, and the PSD of cathode is in the range of 0.85 to 140 nm, hence the L-shape of the contour plots due to the larger maximum pore size in the anode ( $r$  up to 40  $\mu$ m, which is the anode thickness). After 2 h of electrolyte impregnation, Figure 1(a) shows that the electrolyte has not reached to 50% of the cell length from the top; at 25% of the cell length from the top, electrolyte has only infiltrated large macropores above 370 nm in the anode and no pores in the separator and cathode; even the top slice of the cylindrical cell has electrolyte only in pores larger than 10 to 20 nm and electrolyte has not reached any pore sizes smaller than this in the anode and cathode. Electrolyte infiltration under vacuum was set to 1 minute, which is considered as reasonable time for cell production. However, the question is whether the total time for the cell to rest and the electrolyte to continue its impregnation under capillary pressure is sufficient for the electrolyte to fully wet the cell. Clearly, a total impregnation time of 2 h seems insufficient. Figure 1(b) depicts the results for a total electrolyte impregnation time of 24 h, which show that the electrolyte has now reached the bottom of the cell but has wetted only macropores greater than 110 nm at the bottom of the cell. The electrolyte impregnation time with the cell under rest was increased to 48 h in Figure 1(c) and 7 days in Figure 1(d). It is demonstrated that after 7 days of cell under rest, the electrolyte has impregnated the cell up to pores of 10 nm in the anode and cathode and 20 nm in the separator, at the bottom of the cylindrical cell. A reason for differences of electrolyte impregnation between the different cell compo-

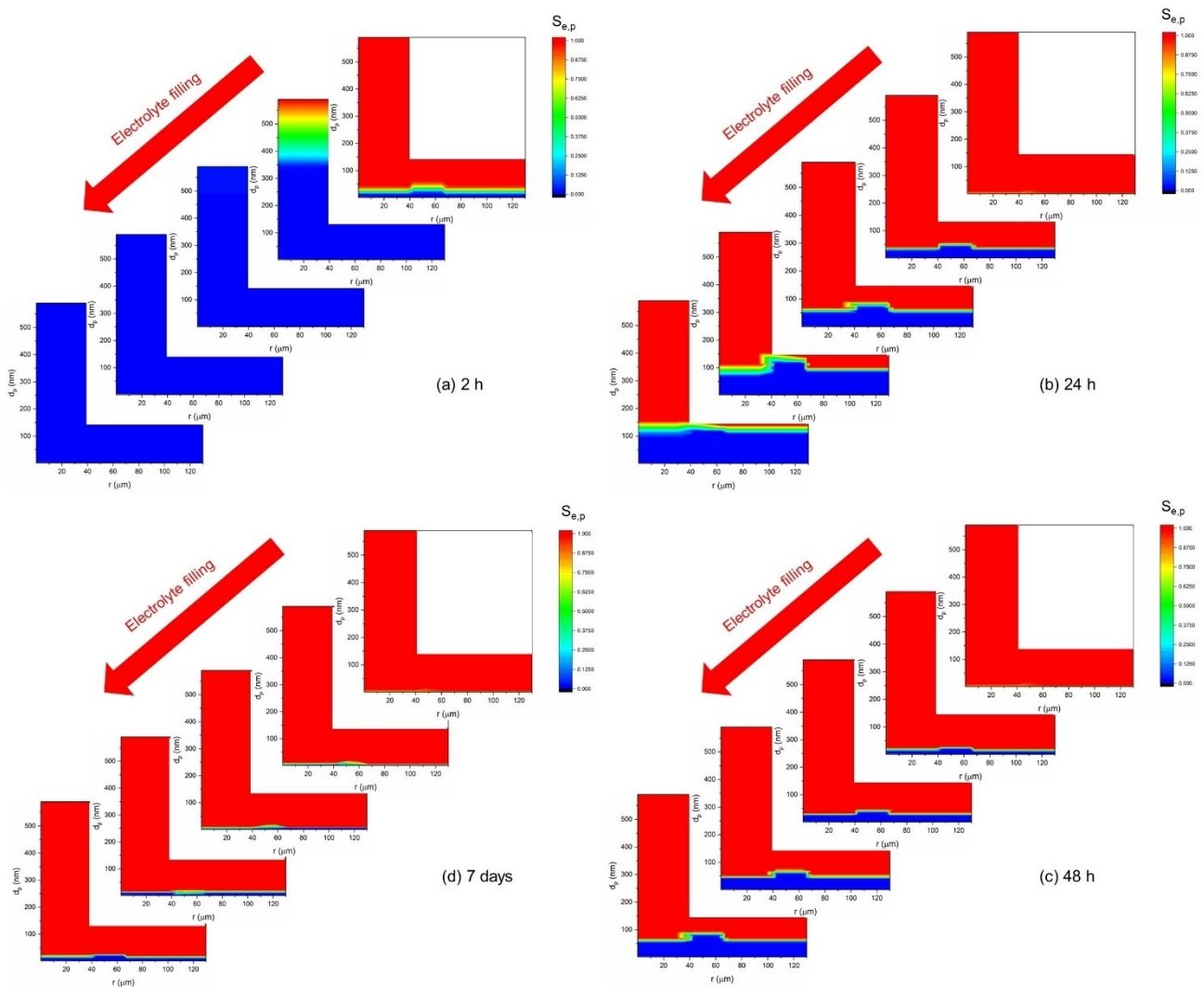


**Figure 1.** Contour plots of the degree of the electrolyte saturation in each pore size,  $S_{e,p}$  in the range of [0 (deep blue) to 1 (red)], as a function of the pore size  $d_p$  and radial distance  $r$  through the cell thickness from anode (40 mm thickness)-to-separator (25 mm thickness)-to-cathode (65 mm thickness) in adjacent electrode layers in a 26650 cylindrical Li-ion cell with electrolyte impregnating from top to bottom, at different distances from the top : 0, 25, 50, 75 and 100%  $x_c$ , with the cell length  $x_c = 65$  mm; for different total time durations of electrolyte impregnation: (a) 2 h, (b) 24 h, (c) 48 h and (d) 7 days.

nents lies in the higher contact angle of the electrolyte with the separator compared to that with the anode and cathode materials. In general, concerning the electrolyte impregnation through different pore sizes in the pore hierarchy, starting from large pores and proceeding to smaller pores, as shown by equation (3), the impregnation speed is proportional to the pore permeability and capillary pressure: the larger pores have higher permeability according to equation (4) but lower capillary pressure according to equation (5). The contact angle between the electrolyte and the porous medium (anode, cathode or separator) also affects the capillary pressure.

Figure SI-2 presents the results of a more refined analysis of the effect of the electrolyte infiltration time, for infiltration times in the range of 1 day to 10 days. It seems that the progress of infiltration into small pores in the lower part of cylindrical cell slows down considerably after 3 days and even more after 7 days. Comparing the results of Figure SI-(i) (10 days) to Figure SI-(g) (7 days), it seems that after 10 days the electrolyte

has reached all pores in the separator, but little progress has been made in the small unfilled pores of anode and cathode since 7 days infiltration time; after 10 days there are still unfilled pores in the electrodes.

The second set of simulations concerns the electrolyte infiltration in the cathode of a Li-S coin cell, where sulfur dissolution or precipitation is also simulated. Figure 2(a) presents the cathode coating microstructure in which cracks are evident creating coating domains simulated as circular with an average diameter of 200  $\mu\text{m}$ . SEM/EDX analysis of the elemental composition around the cracks reveals crack channels of an average width of 30  $\mu\text{m}$  in the carbon host (Figure 2(b2)) with their walls coated with a sulfur layer of 2–10  $\mu\text{m}$  (Figure 2(b3)). Hence, the electrolyte infiltration in the cathode was modeled as two-dimensional transport in notional circular coating domains, progressing from the crack channel towards the center of the circular coating domain and from the top of the

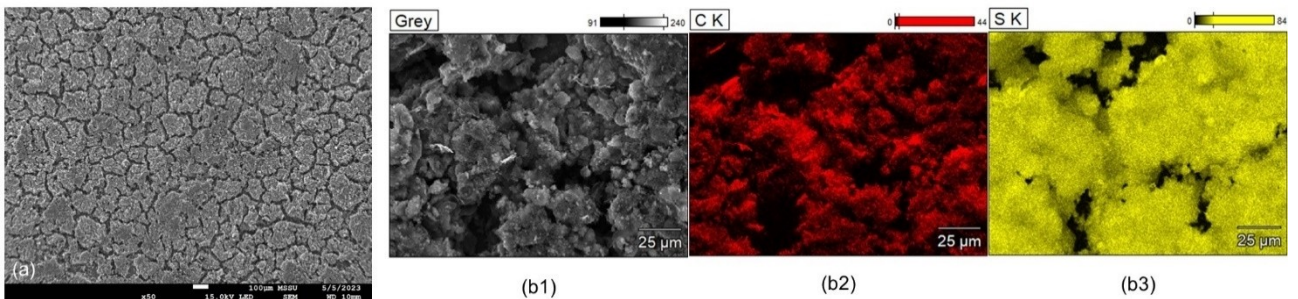


**Figure 2.** SEM/EDX images of cathode coating of Li–S battery: (a) SEM image, size bar = 100 mm; (b1) SEM image, (b2) EDX carbon element map, (b3) EDX sulfur element map, size bar = 25  $\mu$ m.

cathode (where electrolyte was added) to the bottom, by the current collector.

The simulation involved addition of the electrolyte directly on the top of the cathode, at  $E/S = 16 \mu\text{l}/\text{mg}_\text{S}$  (aiming at full saturation), in order to compare the predictions with images from the *in operando* monitoring via microscopy. Figures 3(a1),(b1),(c1) illustrate the progress of the electrolyte infiltration and sulfur dissolution at different times,  $t$ , from the microscope video. At  $t=0$ , the coating is dry with 26.6% crack channels area (white representing the silver-colored aluminium of the current collector foil), determined via image processing as shown in Figure SI-3, and a yellowish grey hue indicating the

presence of sulfur on the carbon particles. 60 s after the addition of electrolyte at the top, the sulfur seems to have dissolved on the top of carbon particles (black hue) and between the particles, so the crack channel area has increased to 36.4% and the initially discontinuous channels are well connected. 200 s after the addition of the electrolyte at the top, the electrolyte has progressed downwards through the thickness of the coating and some sulfur reprecipitation seems to have taken place at the top surface, with the previously black domains losing their intensive black color and the crack channel area decreasing to 31.4%. Figures 3(a2),(b2),(c2) illustrate the predicted progress of sulfur dissolution in the simulation of the

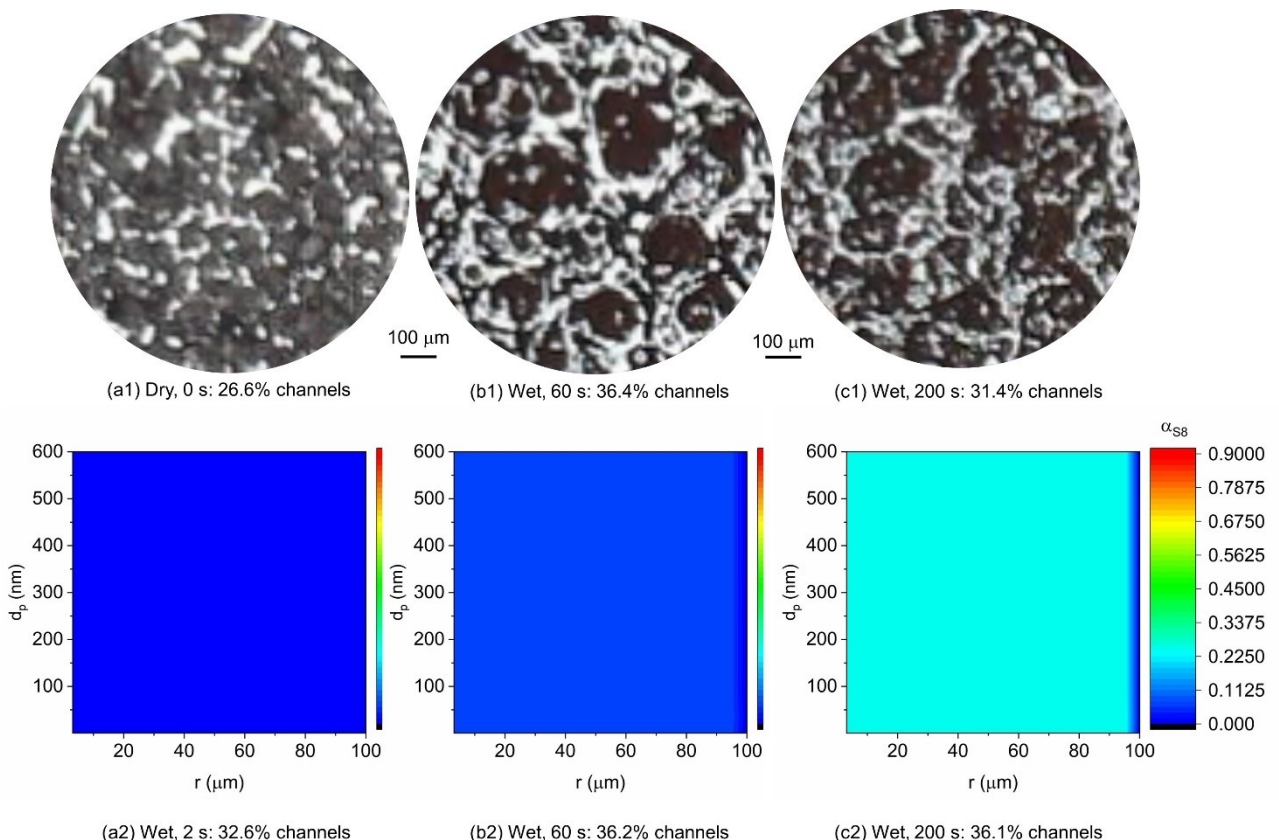


**Figure 3.** Progress of electrolyte infiltration and sulfur dissolution on top surface of sulfur cathode at (a) start, (b) 60 s and (c) 200 s: (a1), (b1), (c1) snapshot images from microscope video monitoring the electrolyte infiltration experiment; (a2), (b2), (c2) contour plots of predicted volume fraction of solid sulfur,  $\alpha_{\text{S}8}$ , on top surface of cathode coating as a function of radial location  $r$  in the notional circular coating domain and the pore size  $d_p$  of the cathode host.

electrolyte infiltration, presenting contour plots of the solid sulfur volume fraction,  $\alpha_{S8}$ , at the top surface of cathode coating as a function of the radial location,  $r$ , in the notional circular coating domain and the pore size of the cathode host. It looks that the addition of electrolyte ( $t=2$  s) leads to sulfur dissolution in both host pores and channel, with the crack area further increasing to 36.2% after 60 s, in agreement with the experimental data. Impregnation of the electrolyte to the lower layers of the cathode coating at 200 s, leaves less electrolyte volume on the top cathode surface, so significant sulfur precipitation is predicted on the top surface of the disc domain, quadrupling the volume fraction  $\alpha_{S8}$  of the precipitated sulfur at 200 s, compared to  $\alpha_{S8}$  at 60 s.

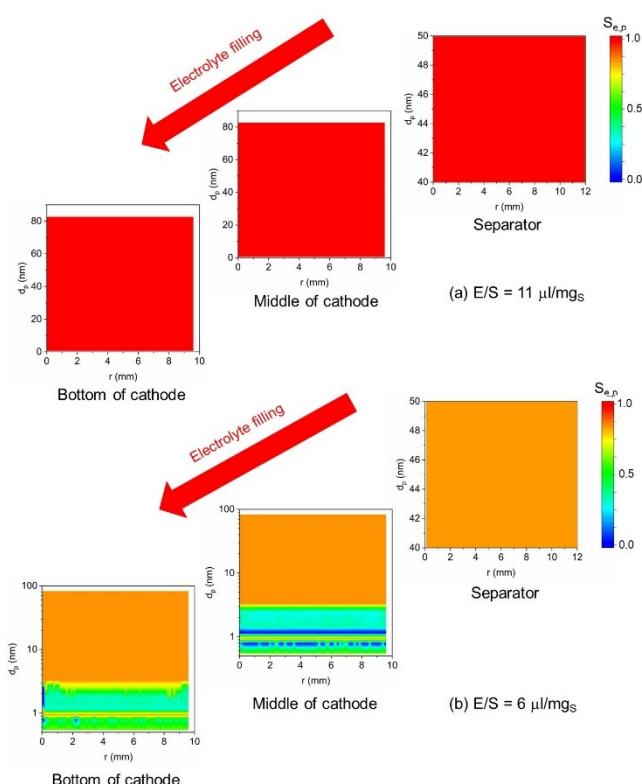
The next set of simulations of the electrolyte infiltration in a Li–S coin cell included both the separator and the cathode, with the electrolyte injected at the top of the separator and the algorithm simulating its infiltration through the separator and subsequently the cathode in two-dimensional flow, in the transverse through-thickness direction and the radial direction, also taking into account the pore size distribution of the cathode and separator, as well as sulfur dissolution or precipitation. The predictions are presented in Figure 4. Two studies were performed at two different electrolyte-to-sulfur ratios:  $E/S=11$  and  $6 \mu\text{l}/\text{mg}_S$ . Starting with a total electrolyte infiltration time of 200 s (as in Figure 3(c1 and c2), Figure 4(a)

demonstrates that cathode and separator are fully saturated with electrolyte homogeneously at all locations and for all pore sizes. The results of Figure 4(a) remained the same in additional simulations, after 1 and 2 hours of electrolyte infiltration. Electrolyte infiltration to 100% saturation across all pores of the cell, is expected for  $E/S=11 \mu\text{l}/\text{mg}_S$  as the volume of added electrolyte in this case is exactly the total pore volume of the cathode host and separator, so these solid porous media would be fully saturated with electrolyte even after all sulfur and sulfides were dissolved in the electrolyte and the total pore volume reached that of the hosts (without sulfur).

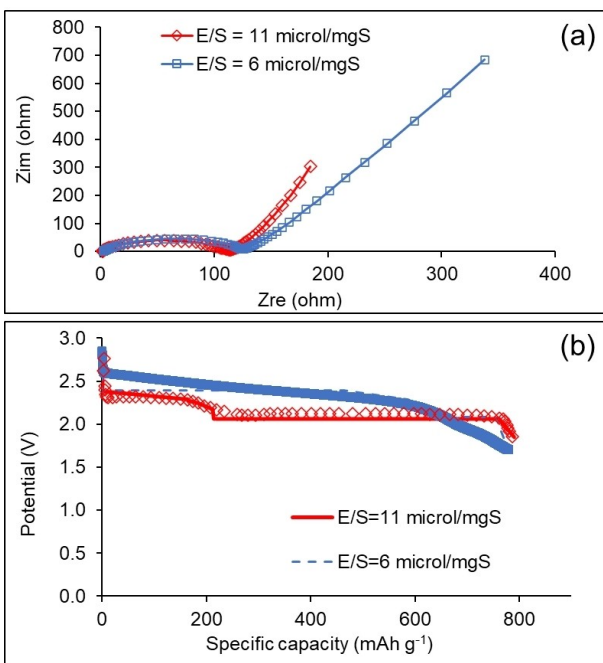
However, for the case of  $E/S=6 \mu\text{l}/\text{mg}_S$  shown in Figure 4(b), the media remain unsaturated, as the total volume of added electrolyte is about 56% of the total pore volume of the cathode host (without any sulfur) and separator. In this case, it is predicted that after 2 hours of electrolyte infiltration the degree of saturation of electrolyte is about 85% in the separator and in any host pore sizes above 3 nm in the cathode. For cathode host pore sizes smaller than 3 nm, the capillary action promoting electrolyte impregnation in small micropores is opposed by the low permeability of these small micropores: the bottom cathode layer by the current collector seems to have electrolyte saturation values from 30 to 85% in the host micropores. The dynamics of sulfur dissolution, transport of the dissolved sulfur and sulfur reprecipitation further affect the actual pore size distribution of the cathode, resulting in some micropore sizes in the middle of the cathode being unwetted by electrolyte, as is shown for the middle transverse location in the cathode in Figure 4(b).

Figure SI-4 illustrates the results of the distribution of the degree of electrolyte saturation in Li–S cells of  $E/S=6 \mu\text{l}/\text{mg}_S$ , after different durations of electrolyte infiltration. Figure SI-4(a) shows that 1 hour of infiltration time is insufficient, as cathode pores of about 1 nm size or less are not reached by the electrolyte at all, especially at the bottom of the cell. This means that during subsequent battery cycling, the lack of electrolyte in micropores would prevent the transport of  $\text{Li}^+$  ions to the micropores, and most particularly through the micropores to the sulfur inside the hollow KB (Ketjenblack EC-600JD) particles. Figure SI-4(b) (same as Figure 4(b)) demonstrates partial saturation of cathode micropores with electrolyte after 2 hours of electrolyte infiltration. Figure SI-4(c) demonstrates that after 3 hours of electrolyte infiltration in the cell, electrolyte distribution has not improved, compared to Figure SI-4(b); in fact, draining is observed in the middle of cathode possibly due to electrolyte redistribution to other locations and sulfur precipitation in key size micropores in this region. In conclusion, 2 hours seems to be the optimum electrolyte infiltration time for the Li–S cell with  $E/S=6 \mu\text{l}/\text{mg}_S$ .

Test data of electrical impedance spectroscopy (EIS) of the two Li–S cells (with  $E/S=11$  and  $6 \mu\text{l}/\text{mg}_S$ ) after been fabricated and left at rest for 2 h for electrolyte infiltration (and pre-GCD cycling) are presented in Figure 5(a). The fully saturated cell at  $E/S=11 \mu\text{l}/\text{mg}_S$  exhibits lower equivalent-in-series resistance  $Z_{\text{re}}$  but higher pore capacitance (lower  $Z_{\text{im}}$ ) than the electrolyte-lean cell at  $E/S=6 \mu\text{l}/\text{mg}_S$ . The lower resistance of the former is due to its better electrolyte wetting and lower void



**Figure 4.** Contour plots of the predicted degree of electrolyte saturation,  $S_{e,p}$ , as a function of the host pore size  $d_p$  and radial distance  $r$ , at different transverse locations in the coin cell, from the separator at the top to the middle and the bottom of cathode for a Li–S battery coin cell: (a) after 200 s electrolyte infiltration time; electrolyte to sulfur ratio  $E/S=11 \mu\text{l}/\text{mg}_S$  and (b) after 2 h electrolyte infiltration time;  $E/S=6 \mu\text{l}/\text{mg}_S$ .



**Figure 5.** Test results of two Li–S battery cells with different E/S ratios ( $E/S = 6 \mu\text{l}/\text{mg}_S$  (unsaturated) and  $11 \mu\text{l}/\text{mg}_S$  (saturated)): (a) experimental EIS test data of the two Li–S cells after fabrication in the form of Nyquist plots of imaginary impedance  $Z_{im}$  versus real impedance  $Z_{re}$ ; (b) discharge curves from the first GCD cycle of the two Li–S cells: series of points curves represent experimental data; thin lines represent model predictions.

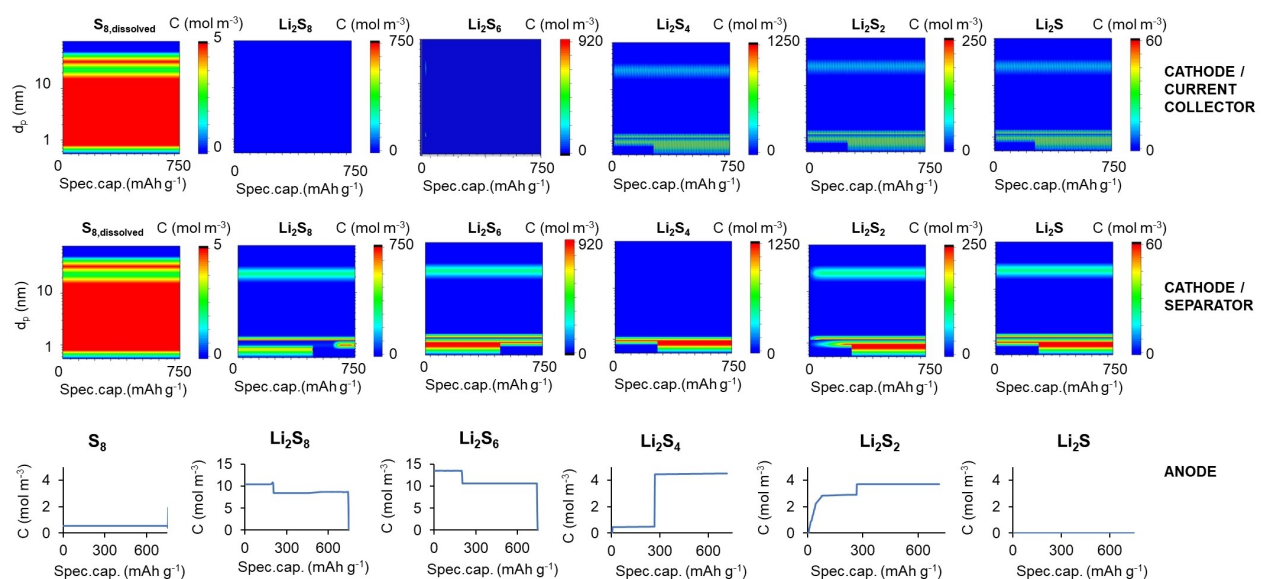
content. However, the differences in the resistance values are small due to the fact that the main source of resistance is the solid sulfur encapsulated in the cathode, which is similar in both cells. However, the excellent pore saturation with electrolyte for the cell with  $E/S = 11 \mu\text{l}/\text{mg}_S$  enhances ion transport in the electrolyte and offers a 2.25x higher pore capacitance for this cell compared to that of the cell with  $E/S = 6 \mu\text{l}/\text{mg}_S$ .

Figure 5(b) displays experimental data (points) and predictions (thin lines) of the voltage variation against the cell specific capacity (with respect to sulfur) for the discharge phase of the first galvanostatic discharge-charge (GCD) cycle for the two Li–S battery cells. Both cells reach similar maximum specific capacity at discharge. The fully saturated cell exhibits a long low voltage plateau, about three times the length of the high voltage plateau, as expected for the final conversion to  $\text{Li}_2\text{S}_2$  and  $\text{Li}_2\text{S}$  at the low plateau, starting with  $\text{Li}_2\text{S}_8$  and continuing with mainly  $\text{Li}_2\text{S}_6$  in the high voltage plateau. The electrolyte-lean cell at  $E/S = 6 \mu\text{l}/\text{mg}_S$  seems to reach the  $\text{Li}_2\text{S}_2$  and  $\text{Li}_2\text{S}$  plateau towards the end of discharge in both experimental data and predictions, with a long linear drop of the high voltage plateau in the experimental data.

The similar overall capacity of the electrolyte-lean cell to the electrolyte-saturated cell in Figure 5(b) seems to be related primarily to the high voltage plateau associated with the production of possibly large amount of  $\text{Li}_2\text{S}_6$  that does not migrate to the anode, reaches the saturation point easily in the low amount of electrolyte in the unsaturated pores and precipitates. The expanded solid content of host pores due to the large volume of precipitated product of higher order

sulfides does not favor the continuous diffusion of  $\text{Li}^+$  ions and conversion to lower sulfides in solid state redox reactions. As a result, the low voltage plateau associated with the production of  $\text{Li}_2\text{S}_2$  and  $\text{Li}_2\text{S}$  is short in the electrolyte-lean cell ( $E/S = 6 \mu\text{l}/\text{mg}_S$ ), due to the high extent of sulfides precipitation in the lean-electrolyte pores in which the saturation point is reached earlier and more easily than in the electrolyte-saturated cell ( $E/S = 11 \mu\text{l}/\text{mg}_S$ ). This means that the shift to solid state  $\text{Li}^+$  ion diffusion slows down the production of  $\text{Li}_2\text{S}_2$  and  $\text{Li}_2\text{S}$  in the electrolyte-lean cell.

Elucidation is provided by the predicted concentration fields of the various dissolved species as a function of the specific capacity during the first discharge in Figures 6 and 7 for Li–S cells with  $E/S = 11$  and  $6 \mu\text{l}/\text{mg}_S$ , respectively. First of all, contour plots of the  $\text{Li}^+$  ion concentration during the first discharge in Figure SI-5(b) (in the cathode by the current collector) reveal the lack of  $\text{Li}^+$  ions in micropores below 2 nm in the electrolyte-lean cell with  $E/S = 6 \mu\text{l}/\text{mg}_S$ , due to the very thin electrolyte layer in these poorly wetted pores (Figure 4(b)). In contrast, the  $\text{Li}^+$  ion concentration contour plot for the cell with  $E/S = 11 \mu\text{l}/\text{mg}_S$  in Figure SI-5(a) illustrates that micropores contain  $\text{Li}^+$  ion concentrations of at least 20 M in the electrolyte. This is replicated by the concentration fields of the dissolved sulfur at two locations in the cathode (by the current collector and by the separator) in Figures 6 and 7, where Figure 7 illustrates that there is no dissolved sulfur in micropores below 2 nm in the electrolyte-lean cell with  $E/S = 6 \mu\text{l}/\text{mg}_S$ . In all contour plots of Figures 6 and 7, the concentration of the dissolved sulfur or sulfides varies from 0 (deep blue) to a maximum (red) which is equal with the saturation concentration of that species in the electrolyte<sup>[14,38]</sup> as precipitation occurs at any greater concentration values. Figure 6 depicts some migration of all species through the cathode and to the anode for the electrolyte-saturated Li–S cell, although migration of the dissolved species to the anode is not so high as for other cathode hosts of a large amount of open pores.<sup>[25]</sup> The limited dissolved sulfur and sulfides migration to the anode in this study is due to the trapping of these species in the hollow KB particles in the cathode host, which reduces the shuttling of polysulfides which is a common problem in Li–S batteries. There is no migration of  $\text{Li}_2\text{S}$  because it precipitates upon its formation in the cathode due to its low solubility.<sup>[14,38]</sup> Sulfur keeps dissolving during the whole discharge and there is still undissolved sulfur at the end of discharge. As a result, the full set of reactions occur during the whole duration of discharge in the electrolyte saturated cell in Figure 6.  $\text{Li}_2\text{S}_2$  and  $\text{Li}_2\text{S}$  are formed in the small micropores in the last  $3/4$  of the discharge, which justifies the long low voltage plateau for this cell in Figure 5(b). In the electrolyte-lean cell ( $E/S = 6 \mu\text{l}/\text{mg}_S$ ) in Figure 7, there is a good amount of  $\text{Li}_2\text{S}_8$  formed in pores from 2 nm and greater in the initial 100  $\text{mAh/g}_S$  of discharge (with an initial high migration to the anode). Thereafter, the discharge is dominated by the formation of  $\text{Li}_2\text{S}_6$  (with negligible migration to the anode) which explains the long high voltage plateau in Figure 5(b).  $\text{Li}_2\text{S}_4$ ,  $\text{Li}_2\text{S}_2$  and  $\text{Li}_2\text{S}$  seem to be formed in the cathode towards the end of discharge in Figure 7, which explains the short low voltage plateau at the end of discharge in Figure 5(b).



**Figure 6.** Predicted concentrations of the dissolved sulfur and sulfides in the electrolyte solution as a function of specific capacity during the first discharge, for Li–S battery cell with  $E/S = 11 \mu\text{l}/\text{mg}_s$ . Contour plots in cathode as a function of pore size  $d_p$  and specific capacity for two different locations (by the current collector and by the separator) and concentration profiles at anode.

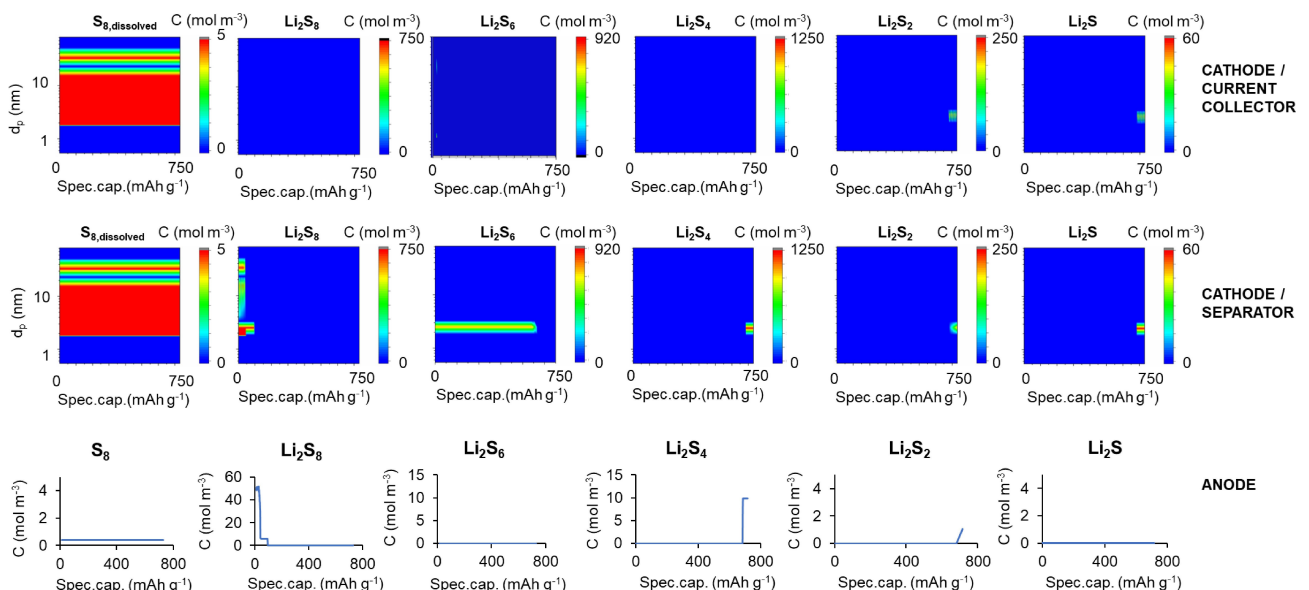


**Figure 7.** Predicted concentrations of the dissolved sulfur and sulfides in the electrolyte solution as a function of specific capacity during the first discharge, for Li–S battery cell with  $E/S = 6 \mu\text{l}/\text{mg}_s$ . Contour plots in cathode as a function of pore size  $d_p$  and specific capacity for two different locations (by the current collector and by the separator) and concentration profiles at anode.

## Conclusions

This study has demonstrated that considerations of the electrolyte impregnation and its effects on the operation of Li-ion and Li–S batteries are essential in the modeling, digital twins and product quality control. We have presented models to simulate the electrolyte infiltration in Li-ion and Li–S battery cells as well as modeling of the operation of a Li–S battery cell with unsaturated porous layers of cathode and separator. Our model

is a continuum-level model taking into account a discretized pore size distribution of the porous medium (cathode, separator or interlayers), which may change during the simulation due to dissolution or precipitation of species such as sulfur or sulfides in sulfur batteries. Electrolyte impregnation and the distribution of the degree of electrolyte saturation throughout the cell and different pore sizes depends on the filling length, the local permeability, which varies as a function of pore size and local degree of compression, and capillary pressure which depends

on the pore size and the wetting properties of the electrolyte for a particular porous medium material.

The format of cell is very important, where it was predicted that a cylindrical Li-ion battery cell may take a week under rest for the electrolyte infiltration to advance to a stage where approximately homogeneous degree of electrolyte saturation is achieved throughout the cylindrical cell length and all the way to the micropores. Electrolyte infiltration with sulfur dissolution and reprecipitation was modeled for Li–S battery cells and the simulation was validated for a coin cell at two electrolyte-to-sulfur ratios: E/S = 11 µl/mg<sub>S</sub> (saturated) and 6 µl/mg<sub>S</sub> (unsaturated). The typical rest time of 2 h for a Li–S coin cell after fabrication was found to be sufficient for the electrolyte to be homogeneously distributed through the cathode for an electrolyte-lean cell, according to the simulation predictions.

The degree of electrolyte saturation throughout the battery cell subsequently affects its operation, with regards to ion transport, precipitation or dissolution of solutes and redox reactions that take place in the liquid electrolyte phase, as in sulfur batteries. Comparing the first discharge of a saturated (E/S = 11 µl/mg<sub>S</sub>) and an electrolyte-lean (E/S = 6 µl/mg<sub>S</sub>) Li–S coin cell, simulation predictions revealed that micropores below 2 nm were poorly wetted for E/S = 6 µl/mg<sub>S</sub>, resulting in poor Li<sup>+</sup> ion transport and sulfur dissolution and, hence, no redox reactions in these pores. Electrolyte-lean cells also experienced more precipitation of sulfides, which offered the advantage of reducing the shuttling of polysulfides but also led to delayed production of Li<sub>2</sub>S<sub>2</sub> and Li<sub>2</sub>S in discharge. High precipitation and low dissolution in electrolyte-lean Li–S cells has the potential to reduce the specific capacity. On the other hand, electrolyte saturated Li–S cells would suffer from more shuttling of polysulfides.

## Experimental Section

Experiments were carried out for Li–S coin cells of 19 mm diameter, with a Li foil anode of 0.75 mm thickness (Sigma Aldrich, UK), separator Celgard 2400 of 25 µm thickness and 25 mm diameter (PSD in Figure SI-1(a)), and a cathode coating on carbon black-coated aluminium foil current collector (MTI, USA). The cathode coating was of 75 µm thickness and consisted of 45.4 wt% sulfur thermally impregnated in cathode host Ketjenblack EC-600JD (Lion Corporation, Japan), of hollow particles of diameter about 30 nm, with 80% hollow core, SSA<sub>BET</sub> = 1415 m<sup>2</sup> g<sup>-1</sup> and PSD presented in Figure SI-1(b).<sup>[25]</sup> Electrolyte was 1 M LiTFSI in DOL/DME 1:1 v/v with also 0.8 M LiNO<sub>3</sub>. Electrochemical testing of cells included electrical impedance spectroscopy (EIS) of the as fabricated Li–S cells (pre-cycling) in a frequency scan from 1 MHz to 10 mHz<sup>[41]</sup> and galvanostatic charge-discharge (GCD) at 0.05 C with respect to the theoretical capacity of sulfur. Scanning electron microscopy (SEM) and energy dispersive X-ray spectroscopy (EDX) were performed on the cathode coating using HR-SEM JEOL-7100F (JEOL Ltd., Tokyo, Japan).

Monitoring of electrolyte infiltration was performed using optical microscopy.<sup>[14,42]</sup> In these experiments, a cathode disc of 10 mm diameter was infiltrated with electrolyte at a ratio E/S = 16 µl/mg<sub>S</sub>. The top surface of the cathode was under an RS PRO digital microscope connected to a PC and operating in video mode. The video was taken for 2 minutes after adding the electrolyte solution

on the top surface of the cathode coating. Snapshot images from selected times in the video were processed using ImageJ.

## Numerical Simulations Section

Electrolyte infiltration was simulated in a 26650 cylindrical cell of graphite-LFP. The system of equations (1)–(5) was solved following a time explicit finite volume/finite difference method.<sup>[43,44]</sup> A numerical grid of 53 (radial direction) x 521 (length direction) points was employed. Discretized PSDs of 22 pore sizes were inputted for the graphite anode and LFP cathode extracted from experimental microstructural data (FIB/SEM) by Scipioni et al (their Figure 8 in [40]), and for Celgard® 2400 separator presented in Figure SI-1(a). The thickness for each layer was: anode of 40 µm,<sup>[40]</sup> cathode of 65 µm<sup>[40]</sup> and separator of 25 µm. The electrolyte was 1 M LiPF<sub>6</sub> in EC/DMC 1:1 v/v of viscosity of 3 mPas, surface tension of 40 mNm<sup>-1</sup>, and contact angle of 22.8° with the graphite anode, 25° with the cathode and 50° with the separator. Electrolyte infiltration took place under vacuum for 1 minute and naturally (under capillary pressure only) thereafter for a total of (a) 2 hours, (b) 24 hours, (c) 48 hours, (d) 3 days (72 hours), (e) 4 days, (f) 5 days, (g) 6 days, (i) 7 days and (j) 10 days.

Electrolyte infiltration and sulfur dissolution or precipitation was simulated for Li–S battery cells of coin cell format, as this is the most common cell format of Li–S battery studies with such batteries being still in developmental stage worldwide. An algorithm solving the system of the full set of equations (1)–(8) was employed using a time explicit finite volume/finite difference method.<sup>[43,44]</sup> A numerical grid of 100 (radial direction) x 10 (transverse direction) points was used with a discretized cathode host PSD of 18 pore sizes. The cathode host was Ketjenblack EC-600JD-based with its PSD determined in.<sup>[25]</sup> The PSDs of the cathode host and the sulfur-host cathode are given in Figure SI-1(b)). The cathode coating was a disc of 19.2 mm diameter and 75 µm thickness, with 45.4 wt% sulfur. The separator was Celgard® 2400 of disc shape of 25 mm diameter and 25 µm thickness. The electrolyte was 1 M LiTFSI in DOL/DME 1:1 v/v of viscosity of 0.5 mPas, surface tension of 28.8 mNm<sup>-1</sup>, and contact angle of 20° with the carbon-sulfur composite cathode and 50° with the separator. Simulations were performed at two alternative E/S ratios: 11 and 6 µl/mg<sub>S</sub>.

These simulations were followed by simulations of the first discharge of each of these two Li–S battery cells (using the dimensions of cells as those used in the experimental section of GCD testing) with different amounts of electrolyte at E/S = 11 or 6 µl/mg<sub>S</sub>. The simulations of discharge at constant current at 0.05 C rate (same as in the experimental section) were performed based on the model of our group presented in [10,25] including equations (9)–(12) updated for unsaturated media. Table SI-1 presents all the equations for the cycling of the Li–S battery cell, employed in this study. In this case, the system of equations is solved via the time implicit finite volume/finite difference method.<sup>[43,44]</sup> Table SI-2 presents the values of the parameters of the dissolution/precipitation model for all species in the Li–S battery cell<sup>[14,38]</sup> and Table SI-3 presents the values of the electrochemical reaction kinetics during the cycling of the Li–S battery cell in the electrolyte used in this study.<sup>[10]</sup>

Contour plots of dependent variables as a function of the pore size and the distance in the cell from the electrolyte infiltration simulations or the specific capacity from the cell discharge simulations were constructed from triads of simulation results via interpolation using graphics software Origin 2020.

## Acknowledgements

This study has been under the umbrella of the LiSTAR project (FIRG014) funded by the Faraday Institute, UKRI grant number EP/S003053/1, and the HiPoBat project funded by EPSRC ISCF Wave 1, grant number EP/R022852/1.

## Conflict of Interests

The authors declare no conflict of interest.

## Data Availability Statement

The data that support the findings of this study are available in the supplementary material of this article.

**Keywords:** electrolyte infiltration · electrolyte-lean batteries · Li-ion batteries · sulfur batteries · simulations

- [1] R. Reece, C. Lekakou, P. A. Smith, *Mater. Sci. Technol.* **2019**, *35*, 368–375.
- [2] A. W. Golubkov, D. Fuchs, J. Wagner, H. Wiltsche, C. Stangl, G. Fauler, G. Voitic, A. Thaler, V. Hacker, *RSC Adv.* **2014**, *4*, 3633–3642.
- [3] J. Marshall, D. Gastrol, R. Sommerville, B. Middleton, V. Goodship, E. Kendrick, *Metals* **2020**, *10*, 773.
- [4] J. P. Baboo, M. A. Yatoo, M. Dent, E. Hojaji Najafabadi, C. Lekakou, R. Slade, S. J. Hinder, J. F. Watts, *Energies* **2022**, *15*, 2332.
- [5] R. Fields, C. Lei, F. Markoulidis, C. Lekakou, *Energy Technol.* **2016**, *4*, 517–525.
- [6] C. Lei, R. Fields, P. Wilson, C. Lekakou, N. Amini, S. Tennison, J. Perry, M. Gosso, B. Martorana, *Proc. Inst. Mech. Eng., Part A* **2021**, *235*, 914–927.
- [7] A. Bhargav, J. He, A. Gupta, A. Manthiram, *Joule* **2020**, *4*, 285–291.
- [8] Z. Li, I. Sami, J. Yang, J. Li, R. V. Kumar, M. Chhowalla, *Nat. Energy* **2023**, *8*, 84–93.
- [9] S. Babar, C. Lekakou, *Ionics* **2021**, *27*, 635–642.
- [10] S. Grabe, M. Dent, S. Babar, T. Zhang, S. Tennison, J. F. Watts, C. Lekakou, *J. Electrochem. Soc.* **2023**, *170*, 020527.
- [11] J. Bates, F. Markoulidis, C. Lekakou, G. M. Laudone, *C* **2021**, *7*, 15.
- [12] F. Markoulidis, J. Bates, C. Lekakou, R. Slade, G. M. Laudone, *Carbon* **2020**, *164*, 422–434.
- [13] C. Sauter, R. Zahn, V. Wood, *J. Electrochem. Soc.* **2020**, *167*, 100546.
- [14] M. Dent, E. Jakubczyk, T. Zhang, C. Lekakou, *J. Phys. Energy* **2022**, *4*, 024001.
- [15] Q. Li, T. Zhang, T. Zhang, Z. Xue, H. Sun, *Energies* **2022**, *15*, 6986.
- [16] M. G. Bader, C. Lekakou, *Processing for laminated structures, in Composites engineering handbook*, (Ed. P. K. Mallick), Marcel Dekker Inc., NY, USA, **1997**, pp. 383–492.
- [17] Z. Deng, Z. Huang, Y. Shen, Y. Huang, H. Ding, A. Luscombe, M. Johnson, J. E. Harlow, R. Gauthier, J. R. Dahn, *Joule* **2020**, *4*, 2017–2029.
- [18] C. Lekakou, S. Cook, Y. Deng, T. W. Ang, G. T. Reed, *Composites Part A* **2006**, *37*, 934–938.
- [19] J. P. Baboo, E. Jakubczyk, M. A. Yatoo, M. Phillips, S. Grabe, M. Dent, S. J. Hinder, J. F. Watts, C. Lekakou, *J. Power Sources* **2023**, *561*, 232762.
- [20] M. Spielbauer, M. Seinhardt, J. Singer, A. Aufschläger, O. Bohlen, A. Jossen, *Batteries* **2023**, *9*, 6.
- [21] D. Di Lecce, V. Marangon, W. Du, D. J. L. Brett, P. R. Shearing, J. Hassoun, *J. Power Sources* **2020**, *472*, 228424.
- [22] S. Amico, C. Lekakou, *Transp. Porous Media* **2004**, *54*, 35–53.
- [23] A. Shodiev, E. Primo, O. Arcelus, M. Chouchane, M. Osenberg, A. Hilger, I. Manke, J. Li, A. A. Franco, *Energy Storage Mater.* **2021**, *38*, 80–92.
- [24] A. Shodiev, F. M. Zanottoa, J. Yu, M. Chouchane, J. Li, A. A. Franco, *Energy Storage Mater.* **2022**, *49*, 268–277.
- [25] S. Grabe, M. Dent, T. Zhang, S. Tennison, C. Lekakou, *J. Power Sources* **2023**, *580*, 233470.
- [26] K. Kumaresan, Y. Mikhaylik, R. E. White, *J. Electrochem. Soc.* **2008**, *155*, A576–A583.
- [27] V. Thangavel, K.-H. Xue, Y. Mamperi, M. Quiroga, A. Mastouri, C. Guery, P. Johansson, M. Morcrette, A. A. Franco, *J. Electrochem. Soc.* **2016**, *163*, A2817–A2829.
- [28] V. Thangavel, O. X. Guerrero, M. Quiroga, A. M. Mikala, A. Rucci, A. A. Franco, *Energy Storage Mater.* **2020**, *24*, 472–485.
- [29] T. Ozgumus, M. Mobedi, U. Ozkol, *Eng. Appl. Comput. Fluid Mech.* **2014**, *8*, 308–318.
- [30] M. Rutt, C. Lekakou, P. A. Smith, A. Sordon, C. Santoni, G. Meeks, I. Hamerton, *Mater. Sci. Technol.* **2019**, *35*, 327–335.
- [31] P. Wang, A. Anderko, R. D. Young, *Ind. Eng. Chem. Res.* **2011**, *50*, 4086–4098.
- [32] C. V. Amanchukwu, X. Kong, J. Qin, Y. Cui, Z. Bao, *Adv. Energy Mater.* **2019**, *9*, 1902116.
- [33] X. Wu, L. Fan, Y. Qiu, M. Wang, J. Cheng, B. Guan, Z. Guo, N. Zhang, K. Sun, *ChemSusChem* **2018**, *11*, 3345–3351.
- [34] J.-Y. Hwang, H. M. Kim, Y.-K. Sun, *J. Electrochem. Soc.* **2018**, *165*, A5006–A5013.
- [35] A. Davoodabadi, J. Li, H. Zhou, D. L. Wood III, T. Singler, C. Jin, *J. Energy Storage* **2019**, *26*, 2352–152X.
- [36] V. V. N. P. Kumar, V. R. Rikka, B. K. Das, G. Raghavan, B. V. A. Rao, R. Prakash, *Ionics* **2019**, *25*, 2549–2561.
- [37] J. P. Baboo, S. Babar, D. Kale, C. Lekakou, G. M. Laudone, *Nanomaterials* **2021**, *11*, 2899.
- [38] H. A. Adeoye, M. Dent, J. F. Watts, S. Tennison, C. Lekakou, *J. Chem. Phys.* **2023**, *158*, 064702.
- [39] Y. Elsayed, C. Lekakou, P. Tomlins, *Polym. Test.* **2014**, *40*, 106–115.
- [40] R. Scipioni, P. S. Jørgensen, C. Graves, J. Hjelm, S. H. Jensen, *J. Electrochem. Soc.* **2017**, *164*, A2017–A2030.
- [41] E. C. Vermisoglou, T. Giannakopoulou, G. Romanos, N. Boukos, V. Psycharis, C. Lei, C. Lekakou, D. Petridis, C. Trapalis, *Appl. Surf. Sci.* **2017**, *392*, 244–255.
- [42] A. K. Murugesh, A. Uthayanan, C. Lekakou, *Appl. Phys. A* **2010**, *100*, 135–144.
- [43] C. N. Lekakou, S. M. Richardson, *Polym. Eng. Sci.* **1986**, *26* (18), 1264–1275.
- [44] Y. Elsayed, C. Lekakou, P. Tomlins, *Biotechnol. Bioeng.* **2019**, *116* (6), 1509–1522.

Manuscript received: July 21, 2023

Revised manuscript received: November 3, 2023

Accepted manuscript online: December 24, 2023

Version of record online: January 25, 2024